Nonlinear mode coupling in a MEMS resonator

Czaplewski, David, López, Daniel, Shoshani, Oriel, Shaw, Steven

David A. Czaplewski, Daniel López, Oriel Shoshani, Steven W. Shaw, "Nonlinear mode coupling in a MEMS resonator," Proc. SPIE 11324, Novel Patterning Technologies for Semiconductors, MEMS/NEMS and MOEMS 2020, 1132414 (23 March 2020); doi: 10.1117/12.2551883

SPIE.

Event: SPIE Advanced Lithography, 2020, San Jose, California, United States

Nonlinear mode coupling in a MEMS resonator

David A. Czaplewski[a,*], **Daniel López**[a], **Oriel Shoshani**[b], **Steven W. Shaw**[c]
[a]Argonne National Laboratory, Center for Nanoscale Materials, 9700 S. Cass Ave., Argonne, IL 60439 USA
[b]Ben-Gurion University of the Negev, Beer-Sheva 84105, Israel
[c]Florida Institute of Technology, Melbourne, FL, 32901, USA

Abstract. A single micro-electromechanical (MEMS) resonator can be shown to exhibit behaviors unexpected in a simple resonant structure. For small driving forces, the resonator displays typical simple harmonic oscillator response. As the driving force is increased, the resonator shows the slightly more complex, but well understood, Duffing response. Rather unexpected response behavior can appear when the resonator frequency is detuned by nonlinearity to where two oscillatory modes of the resonator begin to interact through nonlinear coupling due to an internal resonance. The paper focuses on how the resonator response changes as the internal resonance is approached in the operating parameter space and how that behavior is conveniently represented in a bifurcation diagram. This behavior is accurately captured by a generic mathematical model. We describe an analysis of the model which shows how this coupled response varies with the system and drive parameters, especially focusing on the nonlinear coupling strength between the two modes.

Keywords: MEMS, NEMS, non-linear, resonance, bifurcation diagram, mode coupling, coupling strength.

*David A. Czaplewski, dczaplewski(at)anl.gov

1 Introduction

Resonant MEMS and NEMS structures are used in a wide variety of fields, including force[1–6] and mass sensing,[7–11] timing and frequency control[12,13] and quantum information science.[14–16] In the majority of these applications, the resonant structures have been restricted to operate with a linear response. The primary reasons behind this limitation is to eliminate noise from non-linear effects, to reduce mixing and modulations, and to manage the dynamic range of the response. However, in recent years, more focus has been placed on operating a resonator in its nonlinear range. Benefits have been found in applications with non-linear resonators, including simplified operation of resonant structures in closed-loop operation,[17] increased synchronization range,[18] and frequency tuning of the nonlinear mode.[19] One of the biggest benefits of frequency tuning of a nonlinear mode is to simplify the process of creating nonlinearly coupled modes in a resonator. Mode coupling, in turn, has many interesting and unexpected consequences, including improved phase and frequency

Novel Patterning Technologies for Semiconductors, MEMS/NEMS and MOEMS 2020,
edited by Martha I. Sanchez, Eric M. Panning, Proc. of SPIE Vol. 11324, 1132414
 · doi: 10.1117/12.2551883

stability of oscillators,[20,21] enhanced sensitivity of mass detectors,[22] controlled tuning of the rate of energy dissipation to the environment,[23,24] and parametric amplification in inertial measuring devices.[25] Here, we will focus on understanding the response of a nonlinear resonator experiencing mode coupling by describing how the frequency response changes as a function of parameters, including its bifurcation structure. The dynamics of the response are described by two oscillator equations with a single coupling parameter as described in the modeling section below. By varying the coupling parameter, the model describes how the mode coupling evolves from a relatively simple single mode nonlinear resonance to the complicated coupled mode response observed in the experiments.

2 Experiment

The MEMS resonator used for this research is fabricated from single crystal silicon and is comprised of 3 beams mutually attached at their centers to allow for tuning of a flexural and a torsional mode. Each beam is 500 μm long, 3 μm wide, and 10 μm tall (Fig. 1a). For force actuation and signal transduction, the resonator has a pair of comb drives, one on each side, at the center of the beams. The resonator is operated in a vacuum chamber to reduce air damping. To characterize the response, an output voltage from a lock-in amplifier is applied to one of the comb drives. The signal from the opposite comb drive is sent to a transimpedance amplifier and then a second stage voltage amplifier and then input into the lock-in amplifier. The frequency and amplitude of an applied harmonic voltage are varied to explore the device dynamic response. The linear response of the resonator is characterized by an in-plane flexural mode with $f_{\text{flex}} = 64850$ Hz and linear decay rate of $\Gamma_{\text{flex}} = 0.6$ Hz (Fig. 1b), and a higher order out-of-plane torsional mode with $f_{\text{tor}} = 199599$ Hz and $\Gamma_{\text{tor}} = 1.6$ Hz (Fig. 1c). A schematic of the resonator deformation for each mode is shown

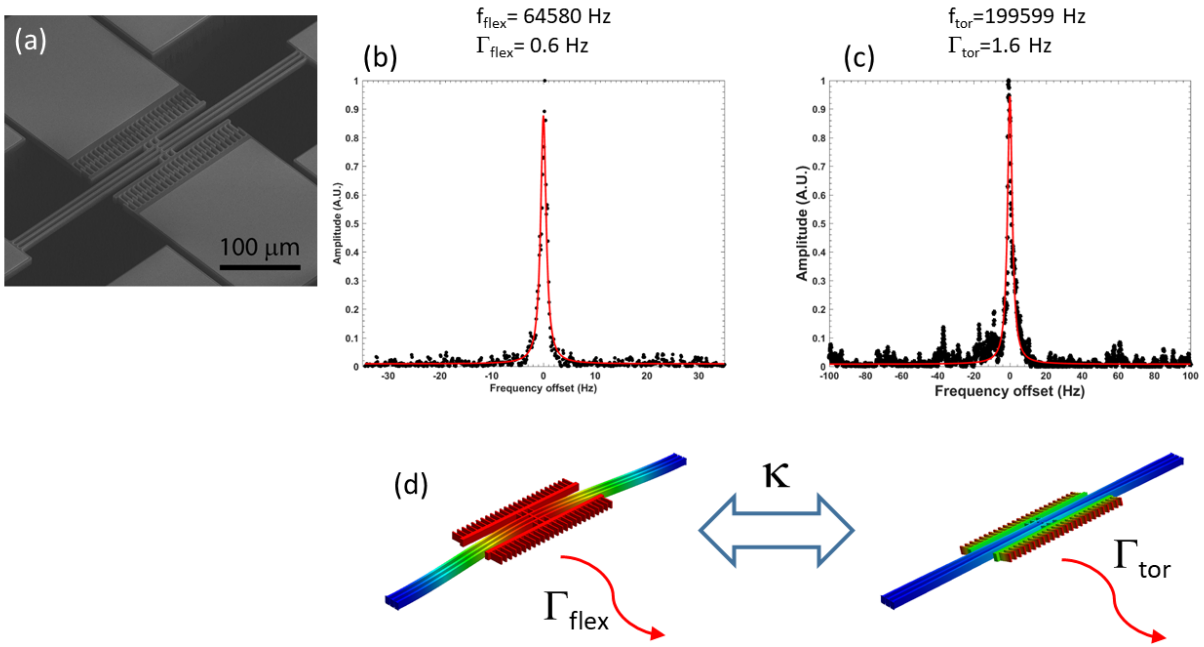

Fig 1 MEMS resonator and characterization. (a) Scanning electron micrograph of the MEMS resonator. (b) Voltage response of the flexural mode of the resonator in its linear range. (c) Voltage response of the torsional mode of the resonator in its linear range. (d) Schematic showing the two resonator modes with their dissipation rates, Γ_{flex} and Γ_{tor}, and coupling strength, κ.

below the frequency responses (Fig. 1d), and the dissipation for each mode and the nonlinear mode coupling are also depicted.

When the drive voltage is increased, the resonator frequency response deviates from the simple harmonic response and follows Duffing behavior.[26] For different driving voltages, different resonant levels of detuning can be achieved, as shown in Fig. 2a. The frequencies at which the resonator response transitions abruptly to the noise floor for different drive voltages are shown by the arrows above each curve. Eventually, for large enough driving voltage, an internal resonance is found to occur at a frequency, f_{IR}, as indicated by the black arrow, at which these jumps accumulate. The creation of a bifurcation diagram (Fig. 2b) from the frequency response of the resonator is described elsewhere.[27] It is important to note that the bifurcation diagram shows various types of stability changes that occur in the parameter plane of the applied voltage amplitude

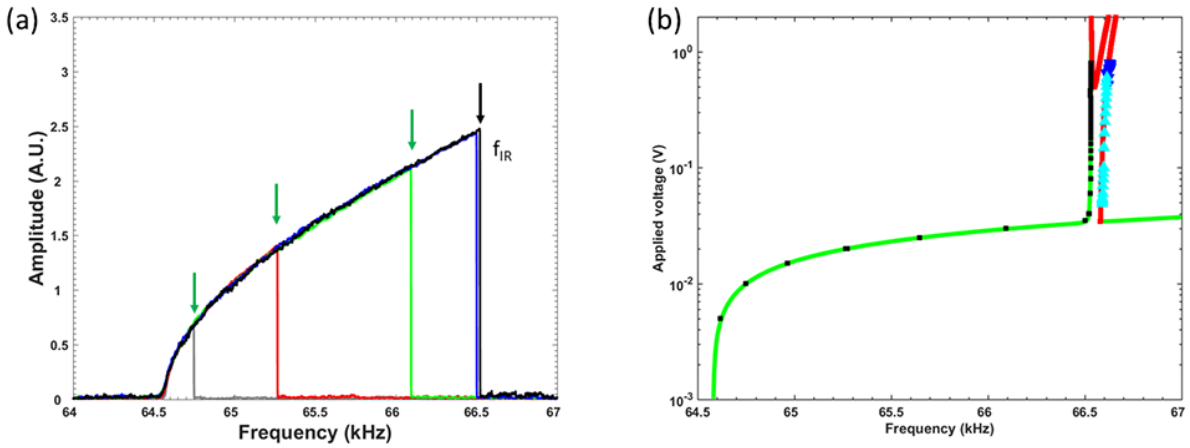

Fig 2 Nonlinear response of a MEMS resonator. (a) Graph showing the response of the MEMS resonator to different levels of applied harmonic voltages (gray: 10 mV, red: 20 mV, green: 30 mV, blue: 40 mV, and black: 50 mV) as the drive frequency is increased. The arrows indicate the frequencies corresponding to an abrupt change in response amplitude of the flexural mode of the resonator. The black arrow is at the frequency of the internal resonance f_{IR}. (b) Graph of the bifurcation conditions indicating qualitative changes in response as a function of drive amplitude and drive frequency. The black squares and blue triangles are the data points represented in (a). The solid green and red lines are obtained from the mathematical model using parameters fitted from the experimental device.

versus frequency. The curves are obtained from the model described below and indicate predicted qualitative changes in the response, and the symbols show corresponding experimental data points, demonstrating the validity and accuracy of the model. The response shown here is significantly different than the linear response plot shown in (Fig. 2a), and from the usual Duffing response, which occurs until the jump point reaches f_{IR}. This difference is represented by the complicated bifurcation pattern seen in the narrow frequency range near f_{IR} in (Fig. 2b) where the red and the vertical green curves are seen to occur above the normal Duffing bifurcation curve (green). The region in frequency space between the vertical green curve on the left, the red curve on the right, and below the red curve on top represents an area in operating space where stable oscillations are not found. This void in operating space is unexpected from such a simple system and could result in significant operating problems if not properly accounted for.

3 Mathematical Model

We consider the essential model that captures the dynamic response of the system. The model is comprised of a Hamiltonian with two vibration modes characterized by coordinates q_k and momenta p_k ($k = 1, 2$). The primary mode ($k = 1$) is a flexural mode and is subjected to harmonic drive and has a quartic Duffing nonlinearity. The secondary mode ($k = 2$) is a torsional mode, which is modeled by a linear harmonic oscillator. The modes are coupled via a nonlinear resonant term that describes the energy exchange between the modes.[26]

$$
\begin{aligned}
H &= H_1 + H_2 + H_{int} + H_F, \\
H_1 &= \frac{1}{2}p_1^2 + \frac{1}{2}\omega_{01}^2 q_1^2 + \frac{1}{6}\omega_1 q_1^4, \quad H_2 = \frac{1}{2}p_2^2 + \frac{1}{2}\omega_{02}^2 q_2^2, \\
H_{int} &= \frac{2}{3}\omega_1 \kappa q_1^3 q_2, \quad H_F = -4\omega_1 q_1 F\cos(\omega_D t).
\end{aligned}
\tag{1}
$$

Linear friction forces are added to each mode and complex amplitudes $A_{1,2}$ are used to describe the amplitudes and phases of the modes relative to a frame of reference that rotates with the harmonic drive. The rotating wave approximation is employed to average out fast oscillations, resulting in a pair of equations in (A_1, A_2) that describe their time evolution on a slow scale related to the relaxation time of the modes.[20] These equations are given by

$$
\dot{A}_1 = -[1 + i(\Delta\omega_1 - |A_1|^2)]A_1 + i\kappa A_2 \bar{A}_1^2 - iF, \tag{2}
$$

$$
\dot{A}_2 = -(\Gamma_{21} + i\Delta\omega_2)A_2 + \frac{i\kappa}{9}A_1^3, \tag{3}
$$

where $\Delta\omega_1 = 2\pi(f_{\mathrm{D}} - f_{\mathrm{flex}})/\Gamma_{\mathrm{flex}}$, $\Delta\omega_2 = 2\pi(3f_{\mathrm{D}} - f_{\mathrm{tor}})/\Gamma_{\mathrm{flex}}$, $\Gamma_{21} = \Gamma_{\mathrm{tor}}/\Gamma_{\mathrm{flex}}$, κ is the normalized coupling parameter, and F is the normalized driving amplitude, which is proportional to the drive voltage V_{o} via a calibration factor (for details see[28]). This model provides a means

of predicting the system response as drive parameters (V_o and f_D) are varied for a given set of device parameters. The stationary response (A_{1s}, A_{2s}) of the coupled system can be found by solving $\dot{A}_{1,2} = 0$. Due to the linearity of the second mode, A_{2s} is easily found to be $A_{2s} = i\kappa A_{1s}^3/9(\Gamma_{21} + i\Delta\omega_2)$, which is essentially a Lorentzian with amplitude dictated by the coupling strength. This is used in the equation for A_{1s} to yield a single implicit expression for A_{1s} in terms of the system and drive parameters,

$$F = i\left[1 + i(\Delta\omega_1 - |A_{1s}|^2) + \frac{\kappa^2|A_{1s}|^4}{9(\Gamma_{21} + i\Delta\omega_2)}\right]A_{1s}. \tag{4}$$

This equation can be used to obtain nonlinear frequency response curves for different drive amplitudes and device parameters. One sees that the flexural mode response, obtained by solving Eq. (4), approaches the standard Duffing response[29] as the coupling term κ tends to zero, while the effects of mode coupling are strongest near the IR, which occurs when $|(\Gamma_{21} + i\Delta\omega_2)|$ is small, namely, when $\Delta\omega_2 \to 0$.

In previous work, the stability of the stationary response was analyzed using a linear stability analysis and considered the behavior of small perturbations to the stationary response.[27] In this analysis, two generic types of instabilities and attendant bifurcations occur. Saddle-node bifurcations are found when two response branches merge and annihilate one another when system or drive parameters are varied. Hopf bifurcations result in periodic modulation of the resonator vibrational amplitude and can be stable or unstable. Saddle-node (green) and Hopf (red) bifurcations are plotted in Fig. 2b, overlaid with the experimental data. The bifurcation values are determined using a the modal coupling coefficient with value $\tilde{\kappa} = 2.964 \cdot 10^{12}\ V^{-2}s^{-2}$.

As is evident from Fig. 2, in the vicinity of the IR (i.e., for drive frequency of nearly one third

of the torsional mode), the response of the flexural mode deviates dramatically from the standard Duffing response of a single mode. Therefore, in the remainder of this section we explore how this anomalous behavior evolves as we vary the coupling parameter κ. For the sake of simplicity we consider only the stationary response of the flexural mode and its saddle-node bifurcations. While this analysis is incomplete, as it ignores the Hopf bifurcations and the fascinating dynamical outcomes that are not stationary responses, it depicts the essential difference in the response curve of the flexural mode due to the resonant interaction with the torsional mode.

From Eq. (4) we find that the stationary magnitude and phase of the steady-state response can be implicitly expressed as

$$|A_{1s}|^2 = \frac{F^2}{\left[1+\frac{\kappa^2\Gamma_{21}}{9(\Gamma_{21}^2+\Delta\omega_2^2)}|A_{1s}|^4\right]^2+\left[\Delta\omega_1-|A_{1s}|^2-\frac{\kappa^2\Delta\omega_2}{9(\Gamma_{21}^2+\Delta\omega_2^2)}|A_{1s}|^4\right]^2}, \tag{5}$$

$$\arg(A_{1s}) = \arctan\frac{1+\frac{\kappa^2\Gamma_{21}}{9(\Gamma_{21}^2+\Delta\omega_2^2)}|A_{1s}|^4}{\Delta\omega_1-|A_{1s}|^2-\frac{\kappa^2\Delta\omega_2}{9(\Gamma_{21}^2+\Delta\omega_2^2)}|A_{1s}|^4}, \tag{6}$$

and the condition for saddle-node bifurcations can be found by requiring[29] that $df_D/d|A_{1s}|^2 = 0$. Starting with a small coupling strength $\kappa \to 0$, we recover the standard Duffing response (Fig. 3, top panel), where from Eq. (5) we can have, at most, three stationary responses for a single frequency [since the equation for the stationary response, Eq. (5), is cubic], a maximal response at $\Delta\omega_1 = |A_{1s}|^2$ where the phase change signs [Eq. (6)], and two saddle-node bifurcation points [the condition for the bifurcation points is a quadratic equation, which stems from the differentiation of Eq. (5)]. As we increase the coupling strength to moderate and large values (Fig. 3, middle and bottom panels), we see that the small divisor $\kappa^2/(\Gamma_{21}^2+\Delta\omega_2^2)$ in Eqs.(5)-(6) starts to play a crucial rule when $\Delta\omega_2 \to 0$. Mathematically, the equation for the stationary response [Eq. (5)] is

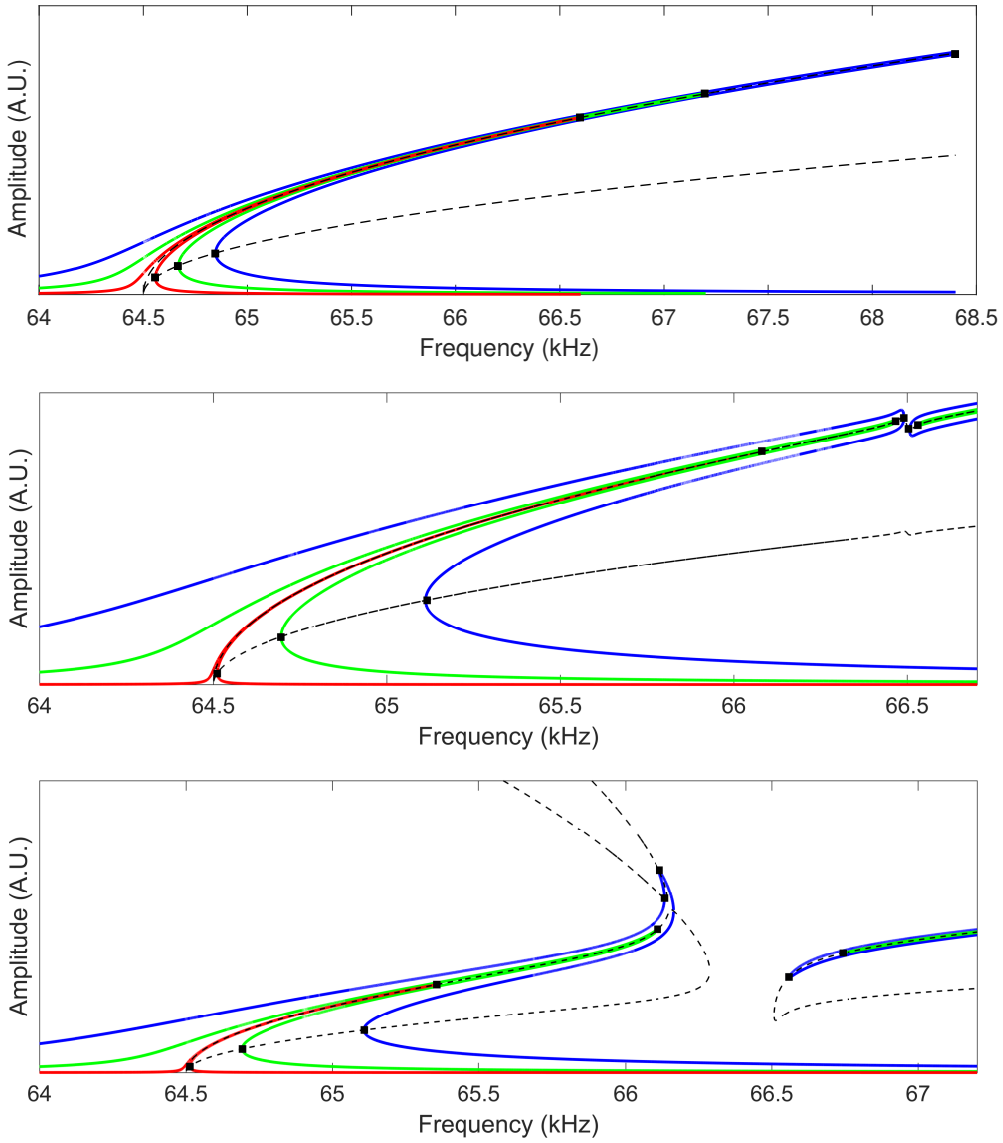

Fig 3 Frequency response curves of the flexural mode for different values of the coupling strength κ. The red, green and blue curves correspond to low, moderate and high drive levels; the loci of the saddle-node bifurcations are indicated by the dashed black curves and are overlaid by the specific bifurcation points (■) of the different drive levels. Top panel—the standard Duffing response for low coupling strength. Middle panel—quasi standard Duffing response for moderate coupling strength, where in the vicinity of the IR there is a small gap in which the response decays to zero (similar to the experimental device). Bottom panel—non-standard Duffing response for high coupling strength, where in the vicinity of the IR there is strong veering of the response resulting in a profound gap with no large amplitude response.

quintic, and therefore, we can have up to five stationary responses for a single frequency, and up to four saddle-node bifurcation points in the response curve. Physically, this phenomenon can be

understood in terms of the Fermi golden rule, where κ is the "matrix element" of the interaction and $1/(\Gamma_{21}^2 + \Delta\omega_2^2)$ is the "density of states" of the effective reservoir provided by the torsional mode at triple the eigenfrequency of the flexural mode, which drains energy from the flexural mode in the vicinity of the IR. It is interesting to note that the response of the flexural mode, which is hardening (that is, the frequency increases with increasing amplitude) when isolated from the torsional mode, can become mixed, going from hardening to softening, when the coupling and drive levels are sufficienly strong.

4 Summary

In this paper, we have described the frequency response of a MEMS resonator with two interacting modes, a flexural mode and a torsional mode, to different levels of harmonic drive. When the device is tuned to an internal resonance via increased driving force amplitude, the response shows behaviors that differ in unexpected ways from a simple oscillator. The coupling at internal resonance creates a void in the operating space of the non-linear resonator due to a mechanism similar to an anti-crossing effect. A minimalistic, nonlinear two-mode model of the system, with a single nonlinear coupling term, is capable of describing the dynamics observed in the experiments. By varying the coupling strength, we showed how the void in the operating space evolves from the expected non-linear Duffing response. In the future, we plan to try to experimentally vary the coupling strength through tunable components of the resonator to further explore the system parameter space.

Acknowledgments

This work was performed, in part, at the Center for Nanoscale Materials, a U.S. Department of Energy Office of Science User Facility, and supported by the U.S. Department of Energy, Office of Science, under Contract No. DE-AC02-06CH11357. SWS is supported by NSF grant 1662619, and SWS and OS are supported by BSF grant 2018041.

References

1 D. Rugar, R. Budakian, H. Mamin, *et al.*, "Single spin detection by magnetic resonance force microscopy," *Nature* **430**(6997), 329 (2004).

2 E. Gavartin, P. Verlot, and T. J. Kippenberg, "A hybrid on-chip optomechanical transducer for ultrasensitive force measurements," *Nature nanotechnology* **7**(8), 509 (2012).

3 J. Moser, J. Güttinger, A. Eichler, *et al.*, "Ultrasensitive force detection with a nanotube mechanical resonator," *Nature nanotechnology* **8**(7), 493 (2013).

4 M. S. Hanay, S. I. Kelber, C. D. O'Connell, *et al.*, "Inertial imaging with nanomechanical systems," *Nature nanotechnology* **10**(4), 339 (2015).

5 R. Decca, D. Lopez, E. Fischbach, *et al.*, "Measurement of the casimir force between dissimilar metals," *Physical Review Letters* **91**(5), 050402 (2003).

6 D. Lopez, R. Decca, E. Fischbach, *et al.*, "Mems-based force sensor: Design and applications," *Bell Labs Technical Journal* **10**(3), 61 (2005).

7 K. Jensen, K. Kim, and A. Zettl, "An atomic-resolution nanomechanical mass sensor," *Nature nanotechnology* **3**(9), 533 (2008).

8 J. Lee, W. Shen, K. Payer, *et al.*, "Toward attogram mass measurements in solution with suspended nanochannel resonators," *Nano letters* **10**(7), 2537–2542 (2010).

9 E. Gil-Santos, D. Ramos, J. Martínez, *et al.*, "Nanomechanical mass sensing and stiffness spectrometry based on two-dimensional vibrations of resonant nanowires," *Nature nanotechnology* **5**(9), 641 (2010).

10 J. Chaste, A. Eichler, J. Moser, *et al.*, "A nanomechanical mass sensor with yoctogram resolution," *Nature nanotechnology* **7**(5), 301 (2012).

11 V. Puller, B. Lounis, and F. Pistolesi, "Single molecule detection of nanomechanical motion," *Physical Review Letters* **110**(12), 125501 (2013).

12 C. Lam, "A review of the recent development of mems and crystal oscillators and their impacts on the frequency control products industry," in *Ultrasonics Symposium, 2008. IUS 2008. IEEE*, 694–704, IEEE (2008).

13 J. Van Beek and R. Puers, "A review of mems oscillators for frequency reference and timing applications," *Journal of Micromechanics and Microengineering* **22**(1), 013001 (2011).

14 S. Kolkowitz, A. C. B. Jayich, Q. P. Unterreithmeier, *et al.*, "Coherent sensing of a mechanical resonator with a single-spin qubit," *Science* **335**(6076), 1603–1606 (2012).

15 T. Palomaki, J. Teufel, R. Simmonds, *et al.*, "Entangling mechanical motion with microwave fields," *Science* **342**(6159), 710–713 (2013).

16 E. Verhagen, S. Deléglise, S. Weis, *et al.*, "Quantum-coherent coupling of a mechanical oscillator to an optical cavity mode," *Nature* **482**(7383), 63 (2012).

17 C. Chen, D. H. Zanette, J. R. Guest, *et al.*, "Self-sustained micromechanical oscillator with linear feedback," *Physical review letters* **117**(1), 017203 (2016).

18 D. Antonio, D. A. Czaplewski, J. Guest, *et al.*, "Nonlinearity-induced synchronization enhancement in micromechanical oscillators," *Physical Review Letters* **114**(3), 034103 (2015).

19 Y. Yang, E. Ng, P. Polunin, *et al.*, "Experimental investigation on mode coupling of bulk mode silicon mems resonators," in *2015 28th IEEE International Conference on Micro Electro Mechanical Systems (MEMS)*, 1008–1011, IEEE (2015).

20 D. Antonio, D. H. Zanette, and D. López, "Frequency stabilization in nonlinear micromechanical oscillators," *Nature communications* **3**, 806 (2012).

21 L. Villanueva, E. Kenig, R. Karabalin, *et al.*, "Surpassing fundamental limits of oscillators using nonlinear resonators," *Physical Review Letters* **110**(17), 177208 (2013).

22 T. Zhang, X. Wei, Z. Jiang, *et al.*, "Sensitivity enhancement of a resonant mass sensor based on internal resonance," *Applied Physics Letters* **113**, 223505 (2018).

23 C. Chen, D. H. Zanette, D. A. Czaplewski, *et al.*, "Direct observation of coherent energy transfer in nonlinear micromechanical oscillators," *Nature communications* **8**, 15523 (2017).

24 J. Güttinger, A. Noury, P. Weber, *et al.*, "Energy-dependent path of dissipation in nanomechanical resonators," *Nature nanotechnology* **12**(7), 631 (2017).

25 S. Nitzan, V. Zega, M. Li, *et al.*, "Self-induced parametric amplification arising from nonlinear elastic coupling in a micromechanical resonating disk gyroscope," *Scientific reports* **5**, 9036 (2015).

26 A. H. Nayfeh and D. T. Mook, *Nonlinear oscillations*, John Wiley & Sons (2008).

27 D. A. Czaplewski, S. Strachan, O. Shoshani, *et al.*, "Bifurcation diagram and dynamic response of a mems resonator with a 1: 3 internal resonance," *Applied Physics Letters* **114**(25), 254104 (2019).

28 D. A. Czaplewski, C. Chen, D. Lopez, *et al.*, "Bifurcation generated mechanical frequency comb," *Physical review letters* **121**(24), 244302 (2018).

29 R. Lifshitz and M. Cross, "Nonlinear dynamics of nanomechanical and micromechanical resonators," *Review of nonlinear dynamics and complexity* **1**, 1–52 (2008).

List of Figures

3 Frequency response curves of the flexural mode for different values of the coupling strength κ. The red, green and blue curves correspond to low, moderate and high drive levels; the loci of the saddle-node bifurcations are indicated by the dashed black curves and are overlaid by the specific bifurcation points (■) of the different drive levels. Top panel—the standard Duffing response for low coupling strength. Middle panel—quasi standard Duffing response for moderate coupling strength, where in the vicinity of the IR there is a small gap in which the response decays to zero (similar to the experimental device). Bottom panel—non-standard Duffing response for high coupling strength, where in the vicinity of the IR there is strong veering of the response resulting in a profound gap with no large amplitude response.